





From Ru-bda to Ru-bds: a step forward to highly efficient molecular water oxidation electrocatalysts under acidic and neutral conditions

Jing Yang^{1,7}, Lei Wang ^{2,7}, Shaoqi Zhan^{3,7}, Haiyuan Zou¹, Hong Chen⁴, Mårten S. G. Ahlquist ³,
Lele Duan ^{1,5}✉ & Licheng Sun ^{2,5,6}✉

Significant advances during the past decades in the design and studies of Ru complexes with polypyridine ligands have led to the great development of molecular water oxidation catalysts and understanding on the O–O bond formation mechanisms. Here we report a Ru-based molecular water oxidation catalyst [Ru(bds)(pic)₂] (**Ru-bds**; bds²⁻ = 2,2'-bipyridine-6,6'-disulfonate) containing a tetradentate, dianionic sulfonate ligand at the equatorial position and two 4-picoline ligands at the axial positions. This **Ru-bds** catalyst electrochemically catalyzes water oxidation with turnover frequencies (TOF) of 160 and 12,900 s⁻¹ under acidic and neutral conditions respectively, showing much better performance than the state-of-art **Ru-bda** catalyst. Density functional theory calculations reveal that (i) under acidic conditions, the high valent Ru intermediate Ru^V=O featuring the 7-coordination configuration is involved in the O–O bond formation step; (ii) under neutral conditions, the seven-coordinate Ru^{IV}=O triggers the O–O bond formation; (iii) in both cases, the I2M (interaction of two M–O units) pathway is dominant over the WNA (water nucleophilic attack) pathway.

¹Department of Chemistry, Shenzhen Grubbs Institute and Guangdong Provincial Key Laboratory of Energy Materials for Electric Power, Southern University of Science and Technology, Shenzhen 518055, People's Republic of China. ²Department of Chemistry, School of Engineering Sciences in Chemistry, Biotechnology and Health, KTH Royal Institute of Technology, 10044 Stockholm, Sweden. ³Department of Theoretical Chemistry & Biology, School of Engineering Sciences in Chemistry, Biotechnology and Health, KTH Royal Institute of Technology, 10044 Stockholm, Sweden. ⁴School of Environmental Science & Engineering, Southern University of Science and Technology, Shenzhen 518055, People's Republic of China. ⁵State Key Laboratory of Fine Chemicals, DUT – KTH Joint Education and Research Center on Molecular Devices, Dalian University of Technology (DUT), Dalian 116012, People's Republic of China. ⁶Center of Artificial Photosynthesis for Solar Fuels, School of Science, Westlake University, 310024 Hangzhou, China. ⁷These authors contributed equally: Jing Yang, Lei Wang, Shaoqi Zhan. ✉email: duanll@sustech.edu.cn; lichengs@kth.se

Artificial photosynthesis is one of the most promising ways to build our society with sustainable energy systems while catalysis of water splitting is the key¹. Two half-reactions are involved in the water-splitting process: water oxidation ($2\text{H}_2\text{O} \rightarrow \text{O}_2 + 4\text{H}^+ + 4\text{e}^-$) and proton reduction ($4\text{H}^+ + 4\text{e}^- \rightarrow 2\text{H}_2$). The first half reaction is widely regarded as the bottleneck of total water splitting. To date, only Ir-based catalysts display high catalytic activity and long durability towards electrochemical water oxidation under strongly acidic conditions^{2,3}. The majority of noble-metal free water oxidation catalysts (WOCs) are confined under strong alkaline conditions whereas they show only moderate performances under neutral conditions and quickly deactivate in acidic media^{4–6}. In contrast, molecular WOCs displayed their advantages over the majority of metal oxides with regard to stability and catalytic activity under acidic conditions. In the last decade, a great number of WOCs based on transition metal complexes such as Fe^{7–9}, Ir¹⁰, Co^{11,12}, Mn^{13,14}, Cu^{15,16} and Ru^{17–20} have been reported, among which Ru-based WOCs with relatively simple polypyridyl ligands are the most representative due to their adequate stability and high catalytic activity under strongly acidic conditions^{21–23}.

Inspired by the first Ru-based WOC, [(bpy)₂(H₂O)Ru^{III}ORu^{III}(OH)₂(bpy)₂](ClO₄)₄ (bpy = 2,2'-bipyridine), reported by Meyer et al. in 1982²⁴, many other Ru WOCs have been developed recently^{25,26}, such as **Ru-Hbpp** (Hbpp[−] = 3,5-bis(2-pyridyl)pyrazolate)²⁷ by Llobet and **Ru-bnp** (bnp = 4-*tert*-Butyl-2,6-di([1',8']-naphthyrid-2'-yl)pyridine) by Thummel²⁸. The mononuclear Ru catalysts, [Ru(bda)(L)₂] (**Ru-bda**; H₂bda = 2,2'-bipyridine-6,6'-dicarboxylic acid; L = N-heterocyclic ligands; Fig. 1), first developed by the Sun group, are among the most efficient molecular WOCs^{17,21}. This type of catalysts catalyze the O–O bond formation via the I2M (interaction of two M–O units) pathway. Later, Llobet and co-workers reported a **Ru-tda** WOC (Fig. 1) with catalytic current density of 4.8 mA/cm² at 1.56 V under pH 7.0 conditions²⁹. Recently, Concepcion and co-workers modified the bda^{2−} ligand by introducing phosphate groups instead of carboxylate groups and prepared complexes **Ru-bpaH₂** (Fig. 1) and [Ru(bpHc)(L)₂] (bpHc^{2−} = 6'-phosphono-[2,2'-bipyridine]-6-carboxylate) with more or less enhanced activity^{30–32}. The **Ru-bda** is very efficient with cerium (IV) ammonium nitrate ((NH₄)₂[Ce^{IV}(NO₃)₆]) as a sacrificial chemical oxidant. However, its electrocatalytic performance is not among the best reported so far. Previous studies on the **Ru-bda** catalysts revealed that electron-withdrawing groups on the axial ligands could enhance water oxidation activity³³.

In this work, by changing the carboxylate ligand to a less electron-donating sulfonate ligand, 2,2'-bipyridine-6,6'-disulfonate (bds^{2−}), we invent a type of highly efficient water oxidation electrocatalyst, [Ru(bds)(pic)₂] (**Ru-bds**; pic = 4-picoline;

Fig. 1), that reaches turnover frequencies (TOF) of 160 and 12900 s^{−1} at pH 1.0 and 7.0 conditions respectively, which outperforms most reported Ru catalysts under similar conditions^{21,29,30}, including the typical **Ru-bda**.

Results and discussion

Synthesis and characterization. The ligand H₂bds was prepared by the nucleophilic substitution of the bromo groups on 6,6'-dibromo-2,2'-bipyridine by NaHS at elevated temperature, followed by the oxidation of the hydrosulfide groups by HNO₃ to obtain the desired sulfonate containing ligand H₂bds. Subsequent coordination of the H₂bds ligand to [Ru(*p*-cymene)Cl₂]₂ in the presence of NEt₃, followed by reaction with 4-picoline yields the corresponding mononuclear catalyst **Ru-bds**. The ¹H/¹³C NMR and ¹H-¹H COSY spectra of H₂bds and **Ru-bds** were shown in Supplementary Figs. 1–8.

The **Ru-bds** crystallizes with two chemically identical but crystallographically distinct molecules in the asymmetric unit. One of the X-ray crystal structures was depicted in Fig. 2, and the Ru centre is in a typical distorted octahedral geometry. It is noticeable that the O3–Ru1–O4 bite angle of **Ru-bds** (114.7(3)°) is slightly larger than that of previously reported **Ru^{III}-bpaH₂** (112.09(6)°)³⁰ whereas smaller than that of **Ru^{II}-bda** (123.0(2)°)¹⁷, all of which are significantly larger than the ideal 90° of an octahedron configuration. The wide O–Ru–O angle provides the open site of the catalyst for substrate water binding and favors the formation of seven-coordinate Ru intermediates during the catalytic process of water oxidation. Noteworthy, as depicted in Supplementary Fig. 9, the C19–C18–C17 angle of 127.1(8)° in **Ru-bds** is a little bit smaller than C8–C7–C6 (129.6(7)°) in **Ru-bda**, showing that the bipyridine ring of **Ru-bds** is less distorted in comparison with that of **Ru-bda**. Thereby, the bds^{2−} ligand backbone fits the Ru^{II} cation slightly better than the bda^{2−} ligand.

The ¹H NMR spectrum of **Ru-bds** in CD₂Cl₂/CD₃OD (Supplementary Fig. 10a) is in agreement with a C_{2v} symmetry of its chemical structure. Two doublets at 8.53 and 8.09 ppm and one triplet at 7.98 ppm were assigned to the proton resonances of the equatorial bds^{2−} ligand while two-resonance peaks at 7.82 and 7.03 ppm to two axial 4-picoline ligands. When the mixed CD₃CN/D₂O was used as the solvent, four broad proton resonances originating from the equatorial ligand appeared while two doublets of the 4-picoline protons remained but slightly downshifted to 8.00 and 7.19 ppm, pointing to a loss of C_{2v} symmetry (Supplementary Fig. 10b). This is attributed to the formation of acetonitrile-coordinating complex, [Ru(k₃^{O,N,N}-bds)(pic)₂(CH₃CN)] with a dangling sulfonate arm. Similar dissociation of the equatorial ligand, such as carboxylate group, was found occurring as well for **Ru-bda**³⁴ and **Ru-pda** (H₂pda is 1,10-phenanthroline-2,9-dicarboxylic acid)³⁵. Labile carboxylate

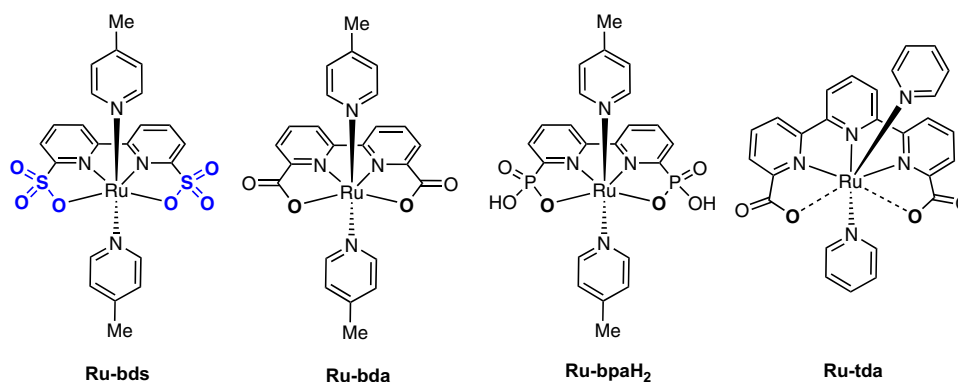


Fig. 1 Structure illustration of complexes. Chemical structures of **Ru-bds**, **Ru-bda**, **Ru-bpaH₂** and **Ru-tda**.

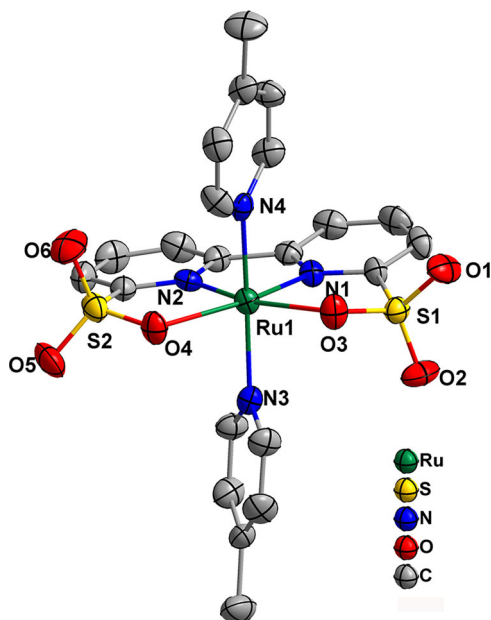


Fig. 2 X-ray crystal structure. The X-ray crystal structure of **Ru-bds** with thermal ellipsoids at 50% probability (hydrogen atoms are omitted for clarity).

chelation is important for water substrate coordinating to the metal center at Ru^{III} states²¹. Thus, the sulfonate chelation in **Ru-bds** should also promote the water coordination to Ru^{III} center and facilitate the further water oxidation steps.

The catalytic performance of this **Ru-bds** under Ce^{IV} -driven water oxidation conditions is less effective but more durable than **Ru-bda** (Supplementary Fig. 11). Kinetic measurements revealed that the oxygen evolution is a first order reaction in regard to both catalyst (Supplementary Fig. 12) and Ce^{IV} (Supplementary Fig. 13) concentrations, meaning that the rate-determining step is an oxidation step, likely $\text{Ru}^{\text{IV}}-\text{OH}$ to $\text{Ru}^{\text{V}}=\text{O}$. The low activity is due to the small driving force of Ce^{IV} ($E(\text{Ce}^{\text{IV}/\text{III}}) = 1.6 \text{ V}$ vs. NHE³⁶; all potentials herein are reported versus normal hydrogen electrode, NHE) in comparison with the catalytic onset potential of **Ru-bds** ($E_{\text{onset}} = 1.6 \text{ V}$; *vide infra*). We thereby studied the electrochemical driven water oxidation by **Ru-bds** in the rest of this work.

Electrochemistry under acidic conditions. First, the electrochemistry of **Ru-bda** and **Ru-bds** was studied in pH 1.0 triflic acid aqueous solutions with 20% CH_3CN (to improve the solubility of **Ru-bds**; it should be noted that acetonitrile competes with water accessing the Ru center and thereby suppresses water oxidation activity²³). As shown in Fig. 3a and Supplementary Fig. 14, **Ru-bda** displays three redox waves at 0.89, 1.12 and 1.33 V, which are related to three consecutive metal-based one-electron oxidation processes: $\text{Ru}^{\text{II}}-\text{NCCH}_3 \rightarrow \text{Ru}^{\text{III}}-\text{OH}_2 \rightarrow \text{Ru}^{\text{IV}}-\text{OH} \rightarrow \text{Ru}^{\text{V}}=\text{O}$, respectively. A small increase in the current density of roughly $0.6 \text{ mA}/\text{cm}^2$ in the 1.5–1.8 V zone indicates slow catalytic water oxidation. Nevertheless, a substantial enhancement of catalytic current density was observed from the CV curve of **Ru-bds** under the acidic conditions (Fig. 3a) reaching a value of $1.48 \text{ mA}/\text{cm}^2$ at 1.74 V. The consecutive oxidation processes of **Ru-bds** were assigned according to the potential versus pH diagram (Supplementary Fig. 15; *vide infra*). The first redox wave is clearly visible at 1.18 V, attributed to the single electron process of $\text{Ru}^{\text{II}}-\text{NCCH}_3 \rightarrow \text{Ru}^{\text{III}}-\text{OH}_2$. The second, irreversible oxidation wave at 1.41 V is corresponding to $\text{Ru}^{\text{III}}-\text{OH}_2 \rightarrow \text{Ru}^{\text{IV}}-\text{OH}$. Oxidation of $\text{Ru}^{\text{IV}}-\text{OH}$ to $\text{Ru}^{\text{V}}=\text{O}$

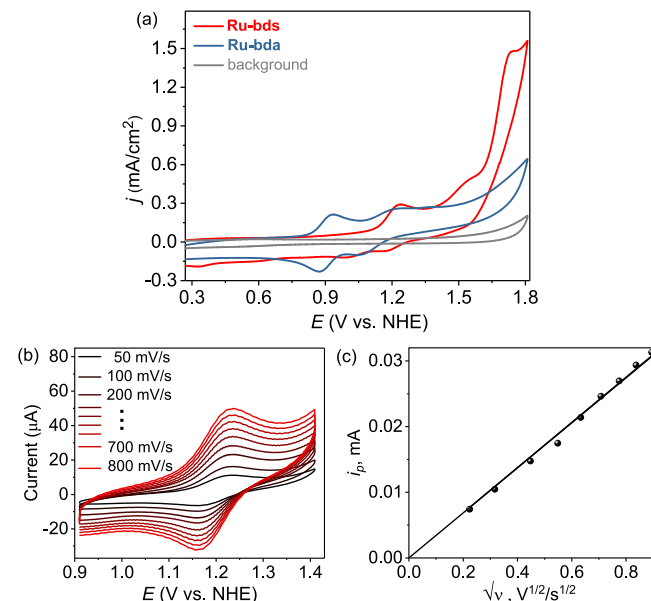


Fig. 3 Electrochemical behavior under acidic conditions. **a** CVs of 1.0 mM **Ru-bda** and **Ru-bds** in pH 1.0 triflic acid aqueous solution containing 20% volume CH_3CN with scan rate of 100 mV s^{-1} (the diameter of glassy carbon working electrode is 3 mm). **b** CV scan rate dependence with 1.0 mM **Ru-bds** from 0.91 to 1.41 V and scan rate varies from 50 to 800 mV s^{-1} . **c** Dependence of the peak current for the $\text{Ru}^{\text{III}/\text{II}}$ couple ($E_{1/2} = 1.18 \text{ V}$) on the square root of scan rate.

(1.58 V) triggers electrochemical water oxidation. All redox states are about 0.3 V higher relative to **Ru-bda**, which is, as expected, due to the relatively less electron-donating ability of the sulfonate group than the carboxylate group.

The $\text{Ru}^{\text{III}/\text{II}}$ redox couples of **Ru-bds** at various scan rates are depicted in Fig. 3b and its peak current (i_p) varies linearly with the square root of scan rate ($v^{1/2}$), indicating a diffusion controlled electrochemical process (Fig. 3c). According to the Randles-Sevcik equation (Eq. 1; F is the Faraday constant, A is the electrode area, $[\text{Ru}^{\text{II}}]$ is the bulk concentration of catalyst, $n_p = 1$ is the number of electrons transferred, $n_{\text{cat}} = 4$ is the number of electrons required to complete a single catalytic cycle, D is the diffusion constant of catalyst, R is the ideal gas constant, and T is the temperature), the diffusion coefficient was $5.02 \times 10^{-6} \text{ cm}^2\text{s}^{-1}$. CV scans of **Ru-bds** and **Ru-bda** at various scan rates are plotted in Fig. 4a,b. The catalytic currents become relatively scan rate independent at 1.5 V s^{-1} for **Ru-bds** and 2.1 V s^{-1} for **Ru-bda**, indicating steady-state conditions are accomplished at such high scan rates. According to the ratio of i_{cat} vs. the noncatalytic Faradaic current (i_p) using an established method with the Eq. 3³⁷, the TOF value of **Ru-bds** is calculated to be 160 s^{-1} at a scan rate of 1.5 V s^{-1} toward electrochemical water oxidation whereas **Ru-bda** displays a TOF of 7 s^{-1} at a scan rate of 2.1 V s^{-1} . Given the above results, **Ru-bds** is surpassing the well-known mononuclear reference **Ru-bda** catalyst towards electrochemical water oxidation under acidic conditions.

$$i_p = 0.446n_pFA[\text{Ru}^{\text{II}}]\left(\frac{n_pFvD}{RT}\right)^{1/2} \quad (1)$$

$$i_{\text{cat}} = n_{\text{cat}}FA[\text{Ru}^{\text{II}}](Dk_{\text{cat}})^{1/2} \quad (2)$$

$$\text{TOF} = 0.1992\left(\frac{Fv}{RT}\right)\left(\frac{n_p^3}{n_{\text{cat}}^2}\right)\left(\frac{i_{\text{cat}}}{i_p}\right)^2 \quad (3)$$

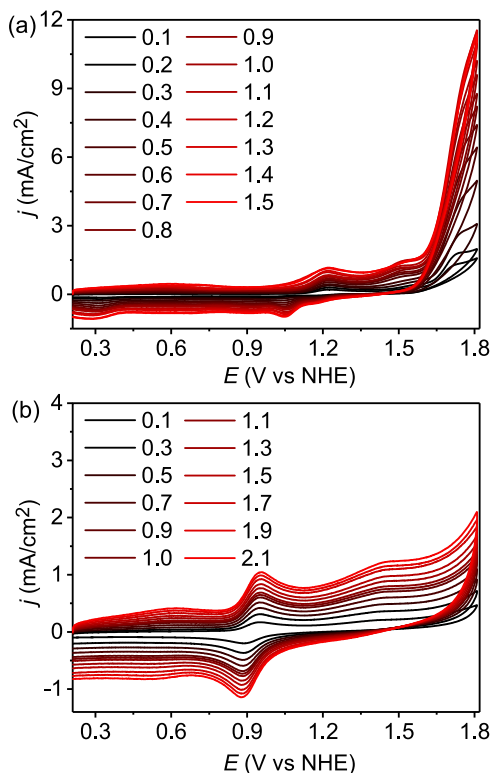


Fig. 4 Electrochemistry under acidic conditions. **a** CVs of **Ru-bds** in pH 1.0/ CH_3CN at different scan rates from 0.1 to 1.5 V s^{-1} . **b** CVs of **Ru-bda** in pH 1.0/ CH_3CN at different scan rates from 0.1 to 2.1 V s^{-1} . Note: i_{cat} values at 1.78 V were used to calculate the TOF for both **Ru-bds** and **Ru-bda**.

To provide more insights into these redox processes and the electronic effect of the equatorial bds^{2-} ligand on the redox properties, the potential versus pH diagram (Pourbaix diagram) of **Ru-bds** was constructed and shown in Supplementary Fig. 15. The potential of the first oxidation step is constant to be ca. 1.18 V up to pH 3.2. The pH independence indicates that only electron transfer is involved in the first oxidation, corresponding to the oxidation of $\text{Ru}^{\text{II}}-\text{NCCH}_3$ to 6-coordinate $\text{Ru}^{\text{III}}-\text{OH}_2$, $[\text{Ru}^{\text{III}}(k_3^{\text{O,N,N}}\text{-bds})(\text{pic})_2(\text{OH}_2)]^+$. Therefore, the pK_a value of $\text{Ru}^{\text{III}}-\text{OH}_2$ was determined to be 3.2, which is much smaller than the pK_a value of 5.5 in **Ru-bda**²¹; this is further in accordance with the relatively poor electron-donating ability of the sulfonate group compared with the carboxylate group. As the pH increases from 3.2 all the way to 8.1, the $\text{Ru}^{\text{III/III}}$ redox couple decreases linearly as the solution pH increases with a slope of -53 mV per pH, corresponding to typical proton-coupled electron transfer (PCET) process and assigned to the oxidation of $\text{Ru}^{\text{II}}-\text{NCCH}_3$ to $\text{Ru}^{\text{III}}-\text{OH}$. For the $\text{Ru}^{\text{IV/III}}$ redox couple, as evidenced by a slope of -64 mV per pH over the range from pH 1.18 to 3.2, the PCET process can be ascribed to the oxidation of $\text{Ru}^{\text{III}}-\text{OH}_2$ to $\text{Ru}^{\text{IV}}-\text{OH}$. Unfortunately, this redox event became too weak to be distinguished at $\text{pH} > 3.0$ and meanwhile it is overlapped with the catalytic current; thereby, the corresponding potential values were obtained by measuring the potential values at 3.0×10^{-5} mA for each scan. The potential of the $\text{Ru}^{\text{IV/III}}$ is constant to be 1.26 V from pH 3.2 to 5.3, which is related to the process of $\text{Ru}^{\text{III}}-\text{OH}$ to $\text{Ru}^{\text{IV}}-\text{OH}$ with only electron transfer. As the pH increase from 5.3 to 8.1, there is a PCET process belonging to the oxidation process of $\text{Ru}^{\text{III}}-\text{OH}$ to $\text{Ru}^{\text{IV}}=\text{O}$. For the $\text{Ru}^{\text{IV}}-\text{OH}$ species produced under acidic conditions, its oxidation via the PCET process leads to the formation of $\text{Ru}^{\text{V}}=\text{O}$, a highly oxidizing state. Additionally, the CV of **Ru-bds** in D_2O containing 0.1 M triflic

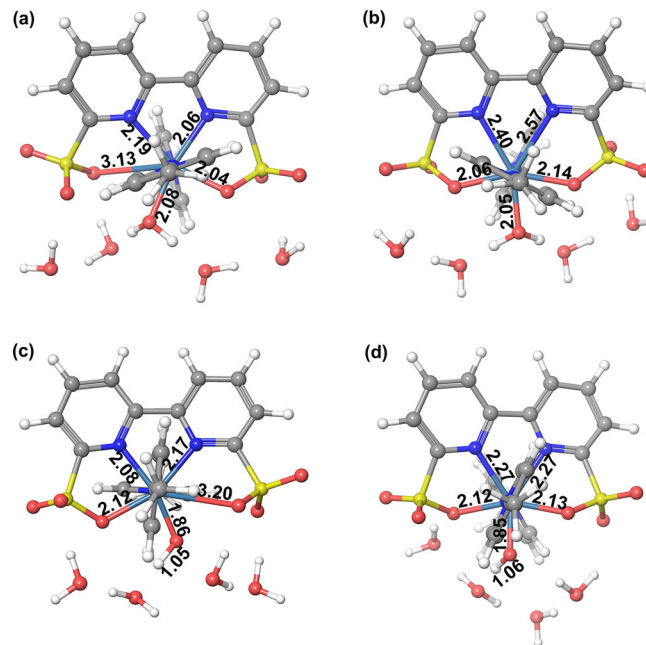


Fig. 5 DFT optimized structures. DFT optimized geometries for the structure conversion of $[\text{Ru}^{\text{III}}-\text{OH}_2]^+$ between **a** 6-coordination and **b** 7-coordination configurations, and $[\text{Ru}^{\text{IV}}-\text{OH}]^+$ between **c** 6-coordination and **d** 7-coordination configurations. The bond lengths are given in Å.

acid was also recorded (Supplementary Fig. 18) and the wave of $\text{Ru}^{\text{III}}-\text{OH}_2$ to $\text{Ru}^{\text{IV}}-\text{OH}$ is too weak to be observed, indicating the slow kinetics of $\text{Ru}^{\text{IV}}-\text{OH}$ formation and thus its low concentration on the electrode surface.

The chronoamperometric curve of **Ru-bds** renders a moderate decay with 42% retention of the initial current density after 2 h bulk electrolysis in pH 1.0 (Supplementary Fig. 19). The corresponding Faradaic efficiency was recorded to be 95%. The post-electrolyzed CVs (Supplementary Fig. 20) demonstrated a two-third peak current loss for $\text{Ru}^{\text{III/III}}$ associated with the catalytic current density declined (from 0.77 to 0.41 mA cm^{-2} at 1.7 V). After bulk electrolysis, **Ru-bds** species is still the dominated species, as shown in the HRMS spectra (Supplementary Figs. 21–24), along with the appearance of several new signals with weak intensity, which are presumably structure-evolved Ru-intermediates and probably contributed to the new redox waves in CVs.

Density functional theory (DFT) calculations. DFT calculations were performed to understand the reason on the high electrochemical driven water oxidation performance of **Ru-bds** and the reaction mechanism behind. As described in the previous study³⁸, four extra water molecules were added around the metal complex to produce a reasonable hydrogen-bonding network. The calculated potential for the couple $[\text{Ru}^{\text{II}}]/[\text{Ru}^{\text{III}}-\text{OH}_2]^+$ at pH 1.0 is 1.15 V, which is close to the experimental value of 1.18 V. Both structures of 6-coordinate $[\text{Ru}^{\text{III}}(k_3^{\text{O,N,N}}\text{-bds})(\text{pic})_2(\text{OH}_2)]^+$ and 7-coordinate $[\text{Ru}^{\text{III}}(\text{bds})(\text{pic})_2(\text{OH}_2)]^+$ were optimized (Fig. 5a, b). The Gibbs free energy of the 6-coordination mode is 6.7 kcal mol^{-1} lower than that of the 7-coordination. The formation of Ru aqua species plays a vital role for water oxidation because it can facilitate further oxidation of the Ru catalyst to higher oxidation states via the PCET process. Upon oxidation of the Ru^{III} aqua species via a PECT process, $[\text{Ru}^{\text{IV}}-\text{OH}]^+$ is formed. The 7-coordinate $[\text{Ru}^{\text{IV}}(\text{bds})(\text{pic})_2(\text{OH})]^+$ (Fig. 5d) becomes more stable than the corresponding 6-coordinate mode $[\text{Ru}^{\text{IV}}(k_3^{\text{O,N,N}}\text{-bds})(\text{pic})_2(\text{OH})]^+$ (Fig. 5c) by a Gibbs free energy difference of

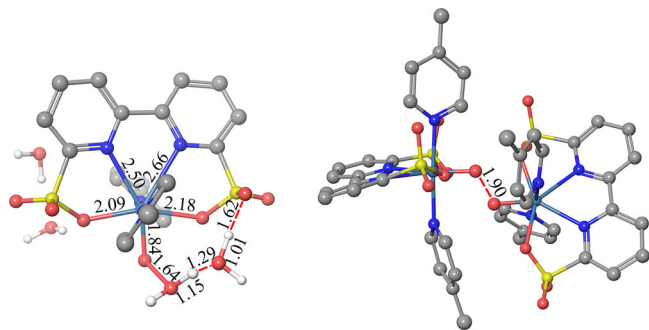


Fig. 6 DFT optimized structures. The transition state structures of WNA (left) and I2M (right) pathway. H atoms except those bonding in water molecules are omitted for clarity. The bond lengths are given in Å.

13.3 kcal mol⁻¹. The corresponding redox potential of [Ru^{III}-OH₂]⁺_{7-coordinate}/[Ru^{IV}-OH]⁺_{7-coordinate} is 1.56 V, which is 0.29 V lower than that of 6-coordinate [Ru^{III}-OH₂]⁺. Further oxidation of [Ru^{IV}-OH]⁺ leads to the formation of [Ru^V=O]⁺ with a calculated oxidation potential of 1.85 V at pH 1.0, compared to the experimental value of 1.58 V.

After the formation of [Ru^V=O]⁺, the O–O bond formation step was calculated via both WNA and I2M pathways (Supplementary Fig. 25) and their corresponding transition states are shown in Fig. 6. The computed activation free energy of the reaction via the WNA pathway is 15.5 kcal mol⁻¹ and the reaction free energy is -3.6 kcal mol⁻¹. For the I2M pathway, the full reaction includes diffusion of two [Ru^V=O]⁺ species, encountering of two [Ru^V=O]⁺ species to form the prereactive dimer and the radical coupling reaction in the full solvent^{39–41}. The computed activation free energy for the radical coupling step is 6.9 kcal mol⁻¹ from the prereactive dimer to the transition state, and the reaction free energy is -11.5 kcal mol⁻¹. The encountering step of two species was found to have a key role for the different catalytic reactivities of **Ru-bda** complexes. We therefore parameterized [Ru^V=O]⁺ model according to our published report⁴¹ and tested stability of the model (Supplementary Fig. 26). Based on the analysis of the hydrogen bonding (Supplementary Fig. 27), the oxo of [Ru^V=O]⁺ of **Ru-bds** is found to be hydrophobic, similar to the oxo of **Ru-bda**. We performed potential of mean force (PMF) simulations to estimate the binding free energy of the prereactive dimer in water phase. The calculated binding free energy of the two [Ru^V=O]⁺ species in water phase is -4 kcal mol⁻¹ (Supplementary Fig. 28), leading to a total activation energy of 2.6 kcal mol⁻¹ for **Ru-bds** (the forward activation free energy of the O–O bond formation minus the free energy of the dissociation of two species; Supplementary Table 2) for the full dimerization. Apparently, the I2M pathway is feasible for **Ru-bds**. In comparison, the activation energy of **Ru-bds** is slightly lower than that of **Ru-bda** (3.9 kcal mol⁻¹)⁴⁰.

Proposed mechanism. On the basis of the above electrochemistry, mass spectrometry, kinetics studies together with DFT calculations, the reaction mechanism of water oxidation by **Ru-bds** under acidic conditions is proposed and depicted in Fig. 7⁴².

Base-enhanced catalytic water oxidation. As shown previously by Meyer and co-workers for the base-enhanced PECT oxidation, the role of the added buffer base was explored by CVs of **Ru-bds** (1.0 mM) at pH 7.0 while maintaining the ionic strength at 0.5 M (compensated by NaNO₃, Supplementary Fig. 31). Significant acceleration of catalytic current is achieved toward water oxidation as the total concentration of H₂PO₄⁻/HPO₄²⁻ buffers increases gradually from 0.01 M to 0.2 M, during which a wave

with nearly plateau shape was observed at the lowest buffer concentration where a maximum current reached at 1.28 V. Therefore, the involvement of the buffer base in PCET pathway directly contributes to the enhanced catalytic activity, which is associated with the electron transferring to electrode occurring along with proton transfer to the added base. CVs were also recorded with different catalyst concentrations at pH 7.0. As the concentration varies from 0.2 mM to 1.0 mM, a sharp enhancement of catalytic current for water oxidation was obtained (Supplementary Fig. 32).

Electrochemistry under neutral conditions. Accordingly, electrochemical behaviors of 1.0 mM **Ru-bds** and **Ru-bda** were further explored in 0.20 M pH 7.0 phosphate buffer solutions (Fig. 8 and Supplementary Fig. 33). To our delight, **Ru-bds** exhibited an ultra-high electrocatalytic current density of 11.79 mA cm⁻² (at 1.63 V with scan rate of 0.1 mV s⁻¹, Fig. 8) with a low onset overpotential of 380 mV. In comparison, the current density of **Ru-bda** is only 3.26 mA cm⁻² (at 1.63 V with scan rate of 0.1 mV s⁻¹, Fig. 8). This significant current density enhancement by **Ru-bds** highlights the importance of PCET in avoiding the high energy barrier for the electrochemical water oxidation. To the best of our knowledge, such a value of the catalytic current density is among the highest ever reported in the literature under neutral conditions for Ru-WOCs catalysed water oxidation (Supplementary Table 3)^{29,30,43,44}. Under the steady-state conditions, a TOF of 12900 s⁻¹ was achieved by **Ru-bds** at the scan rate of 1.3 V s⁻¹ (Fig. 9a) while **Ru-bda** displayed a TOF of 300 s⁻¹ at the scan rate of 2.0 V s⁻¹. The latter is about two orders of magnitude smaller than that of **Ru-bds** (Fig. 9b). Bulk electrolysis of **Ru-bds** in pH 7.0 for 2 h displays a decay with 30% retention of the initial current density (Supplementary Fig. 34a) while the Faradaic efficiency was determined to be 94%. The CVs (Supplementary Fig. 35) show that the Ru^{III/II} peak current retains after bulk electrolysis while the catalytic current density of 8.2 mA cm⁻² only decays to 6.8 mA cm⁻². The two signals of [Ru^{II}(bds²⁻)(pic)₂ + Na]⁺ and [Ru^{II}(bdsNa⁻)(pic)₂(CH₃CN)]⁺ are still the dominate species without formation of new Ru species (Supplementary Figs. 36 and 37).

In our previous study, the mixed-valence Ru trimer species for **Ru-bda**-catalyzed water oxidation under neutral conditions were proved by using chemical and electrochemical methods and have been successfully isolated and characterized⁴⁵. Herein, the spectroelectrochemistry of **Ru-bds** was examined at a constant potential of 1.21 V, where the absorption changes of the electrolysis solution were in situ monitored by UV-Vis spectroscopy. As shown in Supplementary Fig. 38, no observable band at 690 nm was observed where the band at 690 nm is a typical absorption peak of the trinuclear Ru species. Therefore, there is no μ -oxo oligomeric species formed in the case of **Ru-bds**. More importantly, the electrode surfaces before and after electrolysis have also been characterized by scanning electron microscopy (SEM) and energy-dispersive X-ray spectroscopy (EDX) (Supplementary Fig. 39). No Ru elements and species was deposited on the electrode surface, ruling out the potential catalyst decomposition into the RuO₂.

As shown in the Pourbaix diagram, a pH independent oxidation process at 1.0 V appears at pH > 5.5 (grey stars in Supplementary Fig. 15), and this oxidation wave is relatively small compared with the Ru^{III/II} wave (Supplementary Fig. 33). The Ru^{III/II} and Ru^{IV/III} data points respectively aligned well in the whole pH range. Thereby, we propose that the pH independent oxidation process at 1.0 V belongs to a decomposed/evolved Ru species whose structure is currently unknown. Given that, the oxidation of Ru^{III}-OH to Ru^{IV}=O triggers water oxidation with $E_{\text{onset}} = 1.2$ V at pH 7.0.

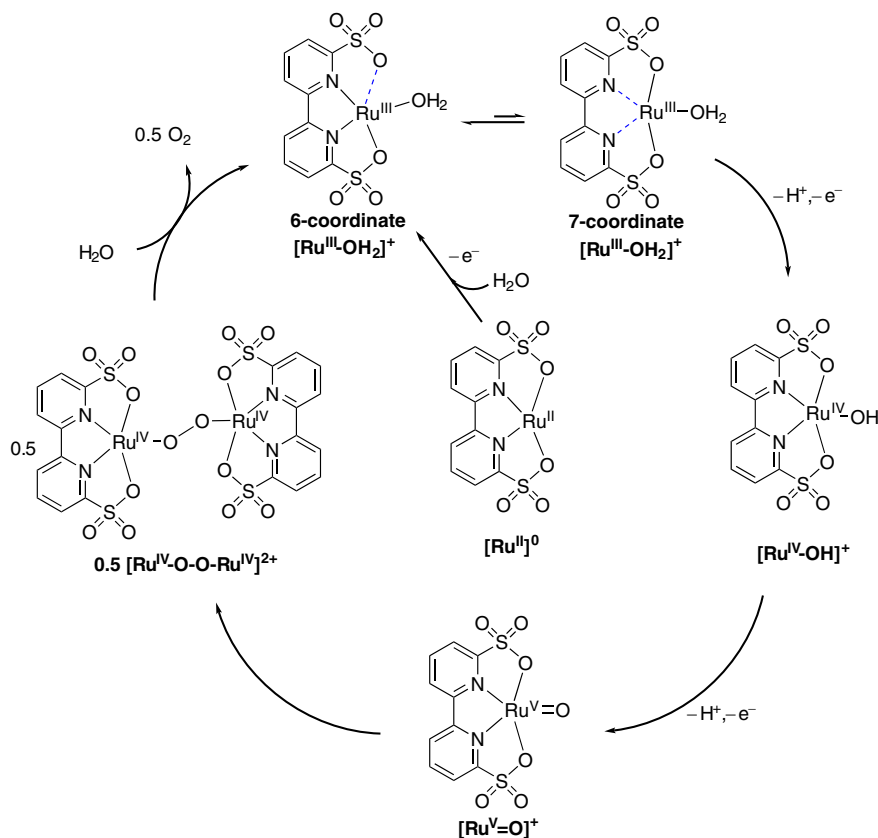


Fig. 7 Proposed mechanism. Proposed electrochemical driven water oxidation and O–O bond formation pathway by **Ru-bds** under the acidic conditions.

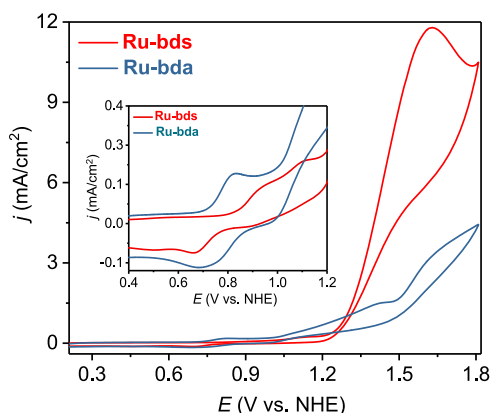


Fig. 8 Electrochemical behavior under neutral conditions. CVs of 1.0 mM **Ru-bda** and **Ru-bds** in pH 7.0 phosphate buffer containing 20% volume CH_3CN with scan rate of 100 mV s^{-1} [0.2 M phosphate buffer, $I = 0.5 \text{ M}$ (NaNO_3)], the diameter of glassy carbon working electrode is 3 mm. Inset: Enlargement of the 0.4–1.2 V zone in the CV.

Density functional theory calculations at pH 7.0. DFT calculations were also performed to gain more insight in the reaction mechanism by **Ru-bds** at pH 7.0. From the Pourbaix diagram, the $\text{Ru}^{\text{III}}\text{-OH}$ will form the $\text{Ru}^{\text{IV}}\text{=O}$ species at $\text{pH} > 4.6$. Calculations showed that the Gibbs free energy of $[\text{Ru}^{\text{III}}\text{-OH}]^+_{(6\text{-coordinate})}$ is only $0.8 \text{ kcal mol}^{-1}$ lower than that of the $[\text{Ru}^{\text{III}}\text{-OH}]^+_{(7\text{-coordinate})}$. In the phosphate buffer, $[\text{Ru}^{\text{IV}}\text{-OH}]^+$ is deprotonated by H_2PO_4^- (dominate species in pH 7.0 phosphate buffer), forming the $\text{Ru}^{\text{IV}}\text{=O}$ (Supplementary Fig. 40) species. Since the Gibbs free energy of $\text{Ru}^{\text{IV}}\text{=O}$ at triplet state is $16.6 \text{ kcal mol}^{-1}$ lower than that of singlet geometry, we

used triplet state of the $\text{Ru}^{\text{IV}}\text{=O}$ species for the calculations. The calculated redox potential of $[\text{Ru}^{\text{III}}\text{-OH}]^+_{(7\text{-coordinate})}/[\text{Ru}^{\text{IV}}\text{=O}]_{\text{T}}$ is 1.08 V at pH 7.0. When the $\text{Ru}^{\text{IV}}\text{=O}$ species form the O–O bond via the WNA pathway using H_2PO_4^- (a stronger base than water) as a proton acceptor, (i) at the triplet state the activation free energy is $51.3 \text{ kcal mol}^{-1}$ and the reaction free energy is $33.9 \text{ kcal mol}^{-1}$ (Fig. 10a), and (ii) at the singlet state the activation free energy is $19.8 \text{ kcal mol}^{-1}$ and the reaction free energy is $15.0 \text{ kcal mol}^{-1}$. Therefore the total activation free energy of WNA pathway is $36.4 \text{ kcal mol}^{-1}$ and the reaction free energy is $31.6 \text{ kcal mol}^{-1}$ (the energy profile at singlet plus the energy difference of $16.6 \text{ kcal mol}^{-1}$ between the singlet and triplet of $\text{Ru}^{\text{IV}}\text{=O}$ species; Fig. 10b).

We have also calculated transition state of radical coupling of two $\text{Ru}^{\text{IV}}\text{=O}$ species by scanning the terminal O–O bond distance $[\text{Ru}^{\text{IV}}\text{=O}\cdots\text{O}=\text{Ru}^{\text{IV}}]$ of the antiferromagnetic open-shell singlet, giving an activation free energy of $6.1 \text{ kcal mol}^{-1}$ from the pre-reactive dimer to the transition state, and a reaction free energy of $1.1 \text{ kcal mol}^{-1}$ (Fig. 10c). We have also parameterized $\text{Ru}^{\text{IV}}\text{=O}_{\text{T}}$ and tested stability by molecular dynamics (MD; Supplementary Fig. 26). The two neutral $\text{Ru}^{\text{IV}}\text{=O}_{\text{T}}$ species are more prone to form the pre-reactive complex with a lower binding free energy of -5 kcal mol^{-1} (Supplementary Fig. 28), compared to the two $[\text{Ru}^{\text{V}}\text{=O}]^+$ species. Therefore the overall activation energy of the O–O bond formation from two separated $\text{Ru}^{\text{IV}}\text{=O}_{\text{T}}$ complexes is only $1.1 \text{ kcal mol}^{-1}$. Further oxidation of $[\text{Ru}^{\text{IV}}\text{=O}]_{\text{T}}$ to form the $[\text{Ru}^{\text{V}}\text{=O}]^+$ however has an oxidation potential of 1.89 V. The high oxidation potential of $\text{Ru}^{\text{V/IV}}$ and the high activation free energy of the WNA pathway indicates that under neutral conditions the O–O bond formation would occur via the I2M pathway at the $\text{Ru}^{\text{IV}}\text{=O}$ state; the I2M pathway at the $\text{Ru}^{\text{IV}}\text{=O}$ state is a new discovery for the molecular based water oxidation catalysis while Meyer and coworkers have

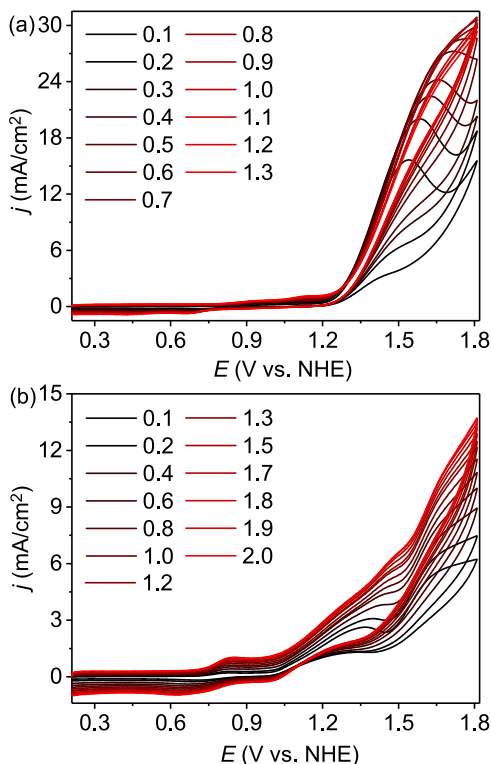


Fig. 9 Electrochemistry under neutral conditions. **a** CVs of **Ru-bds** in pH 7.0 phosphate buffer containing 20% CH_3CN at different scan rates from 0.1 to 1.3 V s^{-1} . **b** CVs of **Ru-bda** in pH 7.0/ CH_3CN at different scan rates from 0.1 to 2.0 V s^{-1} . Conditions: 0.2 M phosphate buffer, $I = 0.5 \text{ M}$ (NaNO_3), glassy carbon working electrode (Φ 3 mm). Note: i_{cat} values at 1.70 V were used to calculate the TOF for both **Ru-bds** and **Ru-bda**.

reported a $\text{Ru}^{\text{IV}}=\text{O}$ catalyzed WNA pathway⁴⁶. Taking the electrochemistry results and theoretical calculations into account, we propose that the rate-limiting step in electrochemical water oxidation by **Ru-bds** at pH 7.0 is the oxidation of $\text{Ru}^{\text{III}}-\text{OH}$ to $\text{Ru}^{\text{IV}}=\text{O}$, and the O–O bond forms via the radical coupling of two $\text{Ru}^{\text{IV}}=\text{O}$ species.

In summary, by introducing two sulfonate groups into a bipyridine ligand, a mononuclear Ru catalyst **Ru-bds** was developed for effective electrocatalytic water oxidation with TOF of 160 s^{-1} under acidic conditions while outstanding catalytic activity with a high TOF of 12900 s^{-1} was successfully obtained under neutral conditions. The bds^{2-} ligand, with the proper electron-donating ability and suitable ligation sites, plays a vital role on stabilizing high valent Ru states, adapting the 7-coordination configuration of reaction intermediates and promoting the O–O bond formation via the I2M mechanism. DFT calculations revealed that the radical coupling of two $\text{Ru}^{\text{IV}}=\text{O}$ species at neutral conditions proceeds with a low activation barrier of $1.1 \text{ kcal mol}^{-1}$, providing a new insight in water oxidation mechanism catalyzed by Ru-based water oxidation catalysts under neutral conditions. In particular, this work illuminates the impact of structural changes on the electrochemical catalytic activity and further provides an inspiring strategy to design more efficient and robust WOCs for potential applications in electrocatalysis and photoelectrocatalysis.

Methods

Physical measurements and instrumentation. Nuclear magnetic resonance (NMR) spectra were obtained with 400 MHz of Bruker Advance spectrometer. Elemental analyses were performed with an Elementar Vario EL elemental analyzer. Mass spectrometry measurements were carried out by a Thermo Scientific

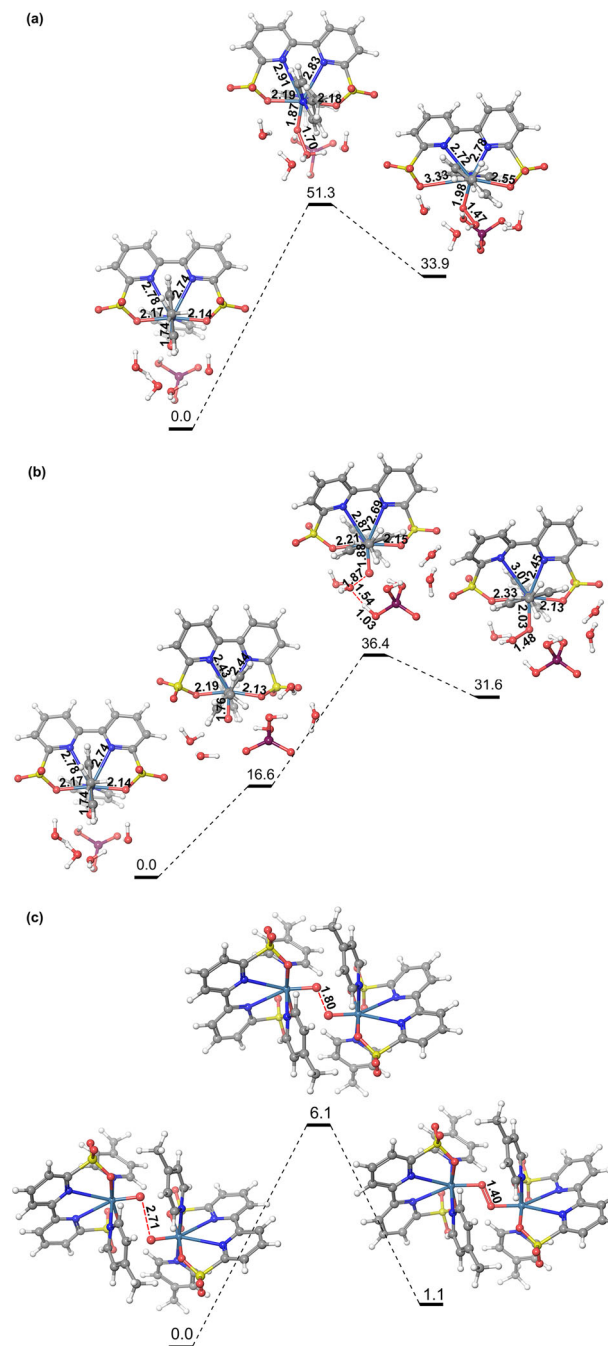


Fig. 10 DFT calculated energy profiles. The energy profiles of O–O bond formation of $\text{Ru}^{\text{IV}}=\text{O}$ at pH 7.0 with the **a** WNA of triplet $\text{Ru}^{\text{IV}}=\text{O}$ using H_2PO_4^- as base, **b** WNA of singlet $\text{Ru}^{\text{IV}}=\text{O}$ using H_2PO_4^- as base, and **c** I2M mechanism. The units of energies are kcal mol^{-1} .

LCQ Fleet mass spectrometer. High-resolution mass spectrometry measurements were performed on a Thermo Scientific Q Exactive mass spectrometer. Electrochemistry measurements were performed with a CHI760 electrochemical workstation. For cyclic voltammetry and differential pulse voltammetry measurements, a glassy carbon disk (diameter 3 mm) was used as the working electrode and a platinum column as the counter electrode, and measured versus Ag/AgCl reference electrode (3 M KCl; 210 mV vs. NHE) in aqueous solutions (conditions: $[\text{cat}] = 1.0 \text{ mM}$; pH 1.0 triflic acid or pH 7.0, 0.2 M phosphate buffer, $I = 0.5 \text{ M}$ (NaNO_3)). For bulk electrolysis, the working electrode was a glassy carbon piece (2.86 cm^2), the counter electrode a platinum wire and the reference electrode a saturated Ag/AgCl electrode (3 M KCl). Typically, 7 mL of 0.5 mM **Ru-bds** in CH_3CN /pH 1.0 or pH 7.0 (0.2 M phosphate buffer) solutions (1/4, v/v) was prepared and the electrolysis current was recorded with an applied potential of 1.7 V at pH 1.0 or 1.5 V at pH 7.0. The electrolytic oxygen evolution in a standard three-electrode H-cell

configuration was monitored by GC9790Plus. The Ce^{IV}-driven oxygen was detected by a pressure transducer (MIK-P300) driven at 10.00 V using a power supply (HY3005B) plus a data acquisition module (Omega OM-DAQ-USB-2401). The single crystal X-ray diffraction data were collected at 298 K on a Bruker SMART CCD 1 K diffractometer with a graphite-monochromated Mo-K_α radiation (λ = 0.71073 Å). The structure was solved and refined using the Olex2 program⁴⁷. Small fraction of twinning domains was suspected in the present datasets. To understand the twinning problem, the twin rotation law has been carefully studied with the Platon software (A.L.Spek, Acta Cryst. 2020, E76, 1–11). The twin law of (−1 0 0 0 −1 −0.36 −0.391 1) has been added into the instruction file for the final refinement. The final refinement has been successfully lower down the refinement R1 value from 8.05 % to 6.71 % with improved residue electron density. A twinning fraction of 4.5 % as founded based on the refinement results. The spectroelectrochemistry was carried out in a Y-shaped quartz cuvette equipped with Pt mesh as working electrode, a Pt wire as counter electrode and an Ag/AgCl reference electrode. The quartz cuvette was filled with 1 mL 0.5 mM Ru-bds in phosphate buffer solution (pH 7, 0.2 M, 20% CH₃CN). The path length of the Y-shaped quartz cuvette is 1.0 mm. UV–vis absorption spectra were obtained by Agilent Technologies Cary 8454. The morphologies of electrode surfaces before and after electrolysis were characterized by a JSM-7500F field emission scanning electron microscopy (SEM, JEOL, Japan).

Synthesis of 2,2′-bipyridine-6,6′-disulfonic acid. To a solution of 6,6′-dibromo-2,2′-bipyridine (312 mg, 1.0 mmol) in dry DMF (8 mL), ten equivalents of sodium hydrosulfide (560 mg, 10 mmol) were added. The reaction mixture was heated under 180 °C for 2 h using Microwave reactor. The resultant orange mixture was dried under vacuum. Dissolve the residue in distilled water, and CH₃COOH was added drop wise until the precipitation stopped. The precipitate was filtered and washed by distilled water, finally dried under vacuum. The product of 6,6′-dithiol-2,2′-bipyridine was afforded as an orange powder (167 mg, 76% yield; its 1D and 2D NMR spectra were recorded to characterize this compound, as shown in Supplementary Figs. 1–2; ¹H NMR (400 MHz, d₆-DMSO) δ 13.67 (s, 2H), 7.47 (dd, J = 8.5, 7.3 Hz, 2H), 7.36 (dd, J = 8.7, 0.9 Hz, 2H), 7.03 (d, J = 6.3 Hz, 2H). HRMS: m/z⁺ = 219.0051 (M + H⁺); calcd, 219.0056, and used for the next step synthesis without further purification. Compound 6,6′-dithiol-2,2′-bipyridine (100 mg) was dissolved in 8 mL nitric acid (70%, purified by redistillation, ≥99.999% trace metals basis), and the solution was heated at 100 °C for 2 h, and then the acid was removed by vacuum. The product of 2,2′-bipyridine-6,6′-disulfonic acid (bdsH₂) was obtained as pale yellow powder in a quantitative yield. Its 1D and 2D NMR spectra were recorded (Supplementary Figs. 3–5). ¹H NMR (400 MHz, D₂O) δ 8.50 (dd, J = 8.0, 0.8 Hz, 2H), 8.20 (t, J = 7.9 Hz, 2H), 8.02 (dd, J = 7.8, 0.7 Hz, 2H). ¹³C NMR (101 MHz, D₂O) δ 161.50, 157.37, 143.05, 127.28, 124.18. HRMS: m/z⁺ = 314.9750 (M + H⁺); calcd, 315.9751. Calcd. for bdsH₂ (C₁₀H₈N₂O₆S₂): C 35.93; H 2.55; N 8.86. Found: C 35.81; H 2.99; N 8.83.

Synthesis of [Ru(bds)(pic)₂]. To a solution of 2,2′-bipyridine-6,6′-disulfonic acid (100 mg, 0.32 mmol) in dry MeOH (5 mL), dichloro(*p*-cymene)ruthenium(II) dimer (98 mg, 0.16 mmol), ten equivalents of 4-picoline and ten equivalents of Et₃N were added. The resulting mixture was then heated under 125 °C for 40 min using a microwave reactor. The solvent was removed by vacuum, and the crude product purified by column chromatography. The target complex was afforded as a dark red powder (65 mg, 35% yield). The 1D and 2D NMR spectra (Supplementary Figs. 6–8) were recorded to characterize the complex. ¹H NMR (400 MHz, mixed CD₃OD and CD₂Cl₂): δ 8.46 (d, J = 8.1 Hz, 2H), 8.09 (d, J = 7.5 Hz, 2H), 7.96 (t, J = 8.0 Hz, 2H), 7.82 (d, J = 6.6 Hz, 4H), 7.03 (dd, J = 6.6, 0.6 Hz, 4H), 2.31 (s, 6H). ¹³C NMR (101 MHz, d₆-DMSO) δ 163.56, 159.57, 151.11, 148.83, 133.94, 126.01, 125.74, 122.68, 20.23. HRMS: calcd for 602.9973 (M + H⁺); found m/z⁺ = 602.9940. Anal. Calcd for [Ru(bds)(pic)₂](C₂₂H₂₀N₄O₆RuS₂): Calcd. C 43.92; H 3.35; N 9.31. Found: C 43.86; H 3.52; N 9.38. Single crystals of Ru-bds was obtained by diffusing diethyl ether into CH₃OH/CH₂Cl₂ (1/5, v/v) solution of complex Ru-bds.

Computational details. All DFT calculations for the estimation of Gibbs free energies were carried out with the Jaguar 8.3 program package by Schrödinger LLC⁴⁸. Molecular geometries were optimized using Becke's three-parameter hybrid functional and the LYP correlation functional (B3LYP)⁴⁹ with D3 correction of Grimme et al.^{50,51} with the LACVP** basis set⁵². Single-point energy corrections were performed with the B3LYP-D3 functional using the LACVP**++ basis set augmented with two f-functions on the metal. Frequency calculations were performed on the optimized geometries to verify that the geometries correspond to minima on the potential energy surface (PES). On the basis of the gas-phase optimized geometries, the solvation energies were estimated by single-point calculations using the Poisson–Boltzmann reactive field implemented in Jaguar (PBF) in water. To identify the transition states for O–O bond formation of I2M mechanism, we searched the potential energy surface by scanning the terminal O–O bond distance [Ru^V=O...O=Ru^V]²⁺ and [Ru^{IV}=O...O=Ru^{IV}] of the antiferromagnetic open shell singlet. The Gibbs free energy were defined as the following equation $G = E(\text{B3LYP-D3/LACVP**++} + 2 \text{ f on Ru}) + G_{\text{sol}} + \text{ZPE} + H_{298} - TS_{298} + 1.9 \text{ kcal/mol}$ (the value 1.9 kcal/mol is a concentration correction to

the free energy of solvation, which by default is calculated at 1 M (g) to 1 M (aq) in Jaguar). Four additional water molecules were included in the calculation.

Force field parameterization. With the optimized geometries of [Ru^V=O]⁺ and Ru^{IV}=O_T, equilibrium bonds, angles, and dihedrals were obtained. Then a series of relaxed coordinate scans were performed by DFT calculations from the equilibrium bonds, angles, and dihedrals to get the force field parameters. Each bond was stretched 0.3 Å in each direction for a total scan span of 0.6 Å, and each angle was stretched 15° in each direction for a total scan span of 30°. The scans were made in 15 increments each way. The scans were fitted to a second-degree polynomial as the following equation where the square term coefficient, k_b , is the force constant.

$$K_b(r - r_0)^2 = K_b r^2 - 2K_b r r_0 + K_b r_0^2$$

The angle parameters have also been plotted with the force constants vs equilibrium angle. Because of the fairly planar structure, most of the dihedral angles have been ignored *i.e.* $K_\psi = 0$, but the dihedral angles that rotates the axial ligand Ru–N bonds have been scanned with the DFT method, and crudely fitted with one cosine series in order to capture the barrier height and equilibrium angles.

Electrostatic potential (ESP) charges were calculated using the DFT method for [Ru^V=O]⁺ (total charge = +1) and Ru^{IV}=O_T (total charge = 0). As an improvement on performing only a single ESP charge calculation, a charge-averaging scheme was implemented, which was performed as follows: 1) Initial ESP charges were calculated at the starting geometry. 2) An MD simulation (gas phase, 300 K, step size 1 fs) was performed starting with the initial structure and charges. A harmonic restraint of 5.0 kcal mol^{−1} was added to Ru atom to restrain it from moving too far from its initial position while the other atoms could move freely during 100 ps of simulation time. A snapshot was extracted every 10 ps of this simulation, at which point new ESP charges were calculated. 3) The procedure was repeated three times, but with the exception that the initial charges of the second and third runs were taken as the average of the ESP charges from the previous run. Each time this procedure was repeated, the charges became more stable, and the procedure was stopped on the third round, when the charges had converged (small standard deviations between the partial charges of the different conformations). All van der Waals parameters used in this work are from the work of Bernardes *et al.*⁵³, where the vdW parameters were determined for M(CO)_n structures for a number for transition metals.

Since [Ru^V=O]⁺ and Ru^{IV}=O_T have the close to identical geometries with different oxidation states, we use same vdW parameters, bond stretch parameters, angle bend parameters, torsion parameters and improper torsion parameters for these two complexes with different calculated average electrostatic potential charges. In order to run MD simulations, the parameters were then transformed into the Gromacs topology format, where the Fourier coefficients of the dihedral potential term were transformed into the Ryckaerd-Bellemans type⁵⁴.

Molecular dynamics simulations. For two MD simulations, the catalyst was sequentially equilibrated in the following order: 1) A 10 ps simulation at 1 K, applying a 5.0 kcal mol^{−1} harmonic restraint on each atom to restrain them to their DFT optimized geometries, and using a 0.1 fs stepsize. 2) A 100 ps simulation at 100 K, applying a 5.0 kcal mol^{−1} harmonic restraint on each atom and increasing to a 1 fs step size. 3) A final 1 ns equilibration at 300 K, reducing the overall harmonic restraint on each atom to 1 kcal mol^{−1} and remaining the stepsize of 1 fs. Solvent was included in the simulations using a 20 Å radius sphere of explicit TIP3P water molecules centered on the centroid of the reacting atoms. The sphere was described as a multi-level system in which the inner 85% of the sphere was allowed to move freely, but all atoms in the last 25% of the sphere were subjected to a 10 kcal mol^{−1} Å^{−2} to maintain system stability, as is routine when using the Surface Constrained All Atom Solvent (SCAAS) model^{55,56}.

Potential of mean force. PMF were performed for the Ru–Ru distance of two complexes in water phase using umbrella sampling method with the Gromacs 5.1.4 MD software package⁵⁷. Equilibrations were performed for 100 ps under an NVT ensemble, using the same methodology described in previous report³⁹. The two Ru complexes were pulled apart for total 10 Å from the core structure over 200 ps, using a spring constant of 30 kJ mol^{−1} Å^{−2} and a pull rate of 0.05 Å ps^{−1}. From these trajectories, snapshots were taken to generate the starting configurations for the umbrella sampling windows. Then we sampled the distances using roughly 0.5 Å spacing. Such spacing allowed for increasing detail at smaller Ru–Ru distance, and resulted in 21 windows. In each window, 20 ns of MD was performed for a total simulation time of 420 ns utilized for umbrella sampling. Analysis of results was performed with the weighted histogram analysis method (WHAM)⁵⁸. All PMF simulations resulted in smooth dissociation curves and the mean value from three repeated simulations.

Data availability

All data needed to evaluate the conclusions of this paper are present in the paper and/or Supplementary Information. The source data underlying Supplementary Figs. 26–29 are provided as a Source Data file. The data that support the findings of this study are available from the corresponding author upon request. The X-ray crystallographic data of Ru-bds reported in this study has been deposited at the Cambridge Crystallographic

Data Center (CCDC), under deposition numbers 1899698 [<https://doi.org/10.5517/ccdc.csd.cc21rs16>]. The data can be obtained free of charge from The Cambridge Crystallographic Data Center via <http://www.ccdc.cam.ac.uk/> data_request/cif. Source data are provided with this paper.

Received: 15 February 2020; Accepted: 14 December 2020;

Published online: 14 January 2021

References

- Berardi, S. et al. Molecular artificial photosynthesis. *Chem. Soc. Rev.* **43**, 7501–7519 (2014).
- Diaz-Morales, O. et al. Iridium-based double perovskites for efficient water oxidation in acid media. *Nat. Commun.* **7**, 12363 (2016).
- Feng, J. R. et al. Iridium-based multimetallic porous hollow nanocrystals for efficient overall-water-splitting catalysis. *Adv. Mater.* **29**, 1703798 (2017).
- Mondschein, J. S. et al. Crystalline cobalt oxide films for sustained electrocatalytic oxygen evolution under strongly acidic conditions. *Chem. Mater.* **29**, 950–957 (2017).
- Hu, F. et al. Amorphous metallic NiFeP: a conductive bulk material achieving high activity for oxygen evolution reaction in both alkaline and acidic media. *Adv. Mater.* **29**, 1606570 (2017).
- Huynh, M., Bediako, D. K. & Nocera, D. G. A functionally stable manganese oxide oxygen evolution catalyst in acid. *J. Am. Chem. Soc.* **136**, 6002–6010 (2014).
- Filloi, J. L. et al. Efficient water oxidation catalysts based on readily available iron coordination complexes. *Nat. Chem.* **3**, 807–813 (2011).
- Wickramasinghe, L. D. et al. Iron complexes of square planar tetradentate polypyridyl-type ligands as catalysts for water oxidation. *J. Am. Chem. Soc.* **137**, 13260–13263 (2015).
- Kotrur, K. G., D'Agostini, S., van Langevelde, P. H., Siegler, M. A. & Hetterscheid, D. G. H. Catalytic activity of an iron-based water oxidation catalyst: substrate effects of graphitic electrodes. *ACS Catal.* **8**, 1052–1061 (2018).
- Bucci, A. et al. An alternative reaction pathway for iridium-catalyzed water oxidation driven by cerium ammonium nitrate (CAN). *ACS Catal.* **6**, 4559–4563 (2016).
- Wang, H. Y., Mijangos, E., Ott, S. & Thapper, A. Water oxidation catalyzed by a dinuclear cobalt-polypyridine complex. *Angew. Chem. Int. Ed.* **53**, 14499–14502 (2014).
- Du, H. Y., Chen, S. C., Su, X. J., Jiao, L. & Zhang, M. T. Redox-active ligand assisted multielectron catalysis: a case of Co-III complex as water oxidation catalyst. *J. Am. Chem. Soc.* **140**, 1557–1565 (2018).
- Ma, L. et al. Cerium(IV)-driven water oxidation catalyzed by a manganese(V)-nitrido complex. *Angew. Chem. Int. Ed.* **54**, 5246–5249 (2015).
- Li, Y. Y., Ye, K., Siegbahn, P. E. M. & Liao, R. Z. Mechanism of water oxidation catalyzed by a mononuclear manganese complex. *ChemSuschem* **10**, 903–911 (2017).
- Koepke, S. J., Light, K. M., VanNatta, P. E., Wiley, K. M. & Kieber-Emmons, M. T. Electrocatalytic water oxidation by a homogeneous copper catalyst disfavors single-site mechanisms. *J. Am. Chem. Soc.* **139**, 8586–8600 (2017).
- Du, J. L., Chen, Z. F., Ye, S. R., Wiley, B. J. & Meyer, T. J. Copper as a robust and transparent electrocatalyst for water oxidation. *Angew. Chem. Int. Ed.* **54**, 2073–2078 (2015).
- Duan, L., Fischer, A., Xu, Y., Sun, L. & Isolated Seven-coordinate Ru(IV) dimer complex with [HOHOH]⁻ bridging ligand as an intermediate for catalytic water oxidation. *J. Am. Chem. Soc.* **131**, 10397–10399 (2009).
- Kunz, V., Schulze, M., Schmidt, D. & Würthner, F. Trinuclear ruthenium macrocycles: toward supramolecular water oxidation catalysis in pure water. *Acc. Energy Lett.* **2**, 288–293 (2017).
- Yu, F. S. et al. Control over electrochemical water oxidation catalysis by preorganization of molecular ruthenium catalysts in self-assembled nanospheres. *Angew. Chem. Int. Ed.* **57**, 11247–11251 (2018).
- Kagalwala, H. N. et al. Evidence for oxidative decay of a Ru-bound ligand during catalyzed water oxidation. *ACS Catal.* **7**, 2607–2615 (2017).
- Duan, L. et al. A molecular ruthenium catalyst with water-oxidation activity comparable to that of photosystem II. *Nat. Chem.* **4**, 418–423 (2012).
- Schulze, M., Kunz, V., Frischmann, P. D. & Würthner, F. A supramolecular ruthenium macrocycle with high catalytic activity for water oxidation that mechanistically mimics photosystem II. *Nat. Chem.* **8**, 576–583 (2016).
- Wang, L., Duan, L., Wang, Y., Ahlquist, M. S. G. & Sun, L. Highly efficient and robust molecular water oxidation catalysts based on ruthenium complexes. *Chem. Commun.* **50**, 12947–12950 (2014).
- Gersten, S. W., Samuels, G. J. & Meyer, T. J. Catalytic oxidation of water by an oxo-bridged ruthenium dimer. *J. Am. Chem. Soc.* **104**, 4029–4030 (1982).
- Duan, L., Wang, L., Li, F., Li, F. & Sun, L. Highly efficient bioinspired molecular Ru water oxidation catalysts with negatively charged backbone ligands. *Acc. Chem. Res.* **48**, 2084–2096 (2015).
- Tong, L. & Thummel, R. P. Mononuclear ruthenium polypyridine complexes that catalyze water oxidation. *Chem. Sci.* **7**, 6591–6603 (2016).
- Sens, C. et al. A new Ru complex capable of catalytically oxidizing water to molecular dioxygen. *J. Am. Chem. Soc.* **126**, 7798–7799 (2004).
- Zong, R. & Thummel, R. P. A new family of Ru complexes for water oxidation. *J. Am. Chem. Soc.* **127**, 12802–12803 (2005).
- Matheu, R. et al. Intramolecular proton transfer boosts water oxidation catalyzed by a Ru complex. *J. Am. Chem. Soc.* **137**, 10786–10795 (2015).
- Xie, Y., Shaffer, D. W., Lewandowska-Andralojc, A., Szalda, D. J. & Concepcion, J. J. Water oxidation by ruthenium complexes incorporating multifunctional bipyridyl diphosphonate ligands. *Angew. Chem. Int. Ed.* **55**, 8067–8071 (2016).
- Shaffer, D. W., Xie, Y., Szalda, D. J. & Concepcion, J. J. Lability and basicity of bipyridine-carboxylate-phosphonate ligand accelerate single-site water oxidation by ruthenium-based molecular catalysts. *J. Am. Chem. Soc.* **139**, 15347–15355 (2017).
- Kamdar, J. M. et al. Ruthenium complexes of 2,2'-bipyridine-6,6'-diphosphonate ligands for water oxidation. *Chemcatchem* **8**, 3045–3049 (2016).
- Duan, L. et al. Insights into Ru-based molecular water oxidation catalysts: electronic and noncovalent-interaction effects on Their catalytic activities. *Inorg. Chem.* **52**, 7844–7852 (2013).
- Song, N. et al. Base-enhanced catalytic water oxidation by a carboxylate-bipyridine Ru(II) complex. *Proc. Natl Acad. Sci. USA* **112**, 4935–4940 (2015).
- Tong, L., Duan, L., Xu, Y., Privalov, T. & Sun, L. Structural modifications of mononuclear ruthenium complexes: a combined experimental and theoretical study on the kinetics of ruthenium-catalyzed water oxidation. *Angew. Chem. Int. Ed.* **50**, 445–449 (2011).
- Nair, V. & Deepthi, A. Cerium(IV) ammonium nitrate - a versatile single-electron oxidant. *Chem. Rev.* **107**, 1862–1891 (2007).
- Ngo, K. T. et al. Turning on the protonation-first pathway for electrocatalytic CO₂ reduction by manganese bipyridyl tricarbonyl complexes. *J. Am. Chem. Soc.* **139**, 2604–2618 (2017).
- Daniel, Q. et al. Rearranging from 6- to 7-coordination initiates the catalytic activity: an EPR study on a Ru-bda water oxidation catalyst. *Coord. Chem. Rev.* **346**, 206–215 (2017).
- Zhan, S. Q., Zou, R. F. & Ahlquist, M. S. G. Dynamics with explicit solvation reveals formation of the prereactive dimer as sole determining factor for the efficiency of Ru(bda)₂ catalysts. *ACS Catal.* **8**, 8642–8648 (2018).
- Zhan, S., Martensson, D., Purg, M., Kamerlin, S. C. L. & Ahlquist, M. S. G. Capturing the role of explicit solvent in the dimerization of Ru^V(bda) water oxidation. *Catalysts. Angew. Chem. Int. Ed.* **56**, 6962–6965 (2017).
- Zhan, S. Q. & Ahlquist, M. S. G. Dynamics and reactions of molecular Ru catalysts at carbon nanotube-water interfaces. *J. Am. Chem. Soc.* **140**, 7498–7503 (2018).
- Lebedev, D. et al. The key Ru^V=O intermediate of site-isolated mononuclear water oxidation catalyst detected by in situ X-ray absorption spectroscopy. *J. Am. Chem. Soc.* **140**, 451–458 (2018).
- Matheu, R. et al. The role of seven-coordination in Ru-catalyzed water oxidation. *ACS Catal.* **8**, 2039–2048 (2018).
- Shatskiy, A. et al. Electrochemically driven water oxidation by a highly active ruthenium-based catalyst. *ChemSuschem* **12**, 2251–2262 (2019).
- Zhang, B. et al. Characterization of a trinuclear ruthenium species in catalytic water oxidation by Ru(bda)(pic)₂ in neutral media. *Chem. Commun.* **52**, 8619–8622 (2016).
- Tamaki, Y., Vannucci, A. K., Dares, C. J., Binstead, R. A. & Meyer, T. J. One-electron activation of water oxidation catalysis. *J. Am. Chem. Soc.* **136**, 6854–6857 (2014).
- Dolomanov, O. V., Bourhis, L. J., Gildea, R. J., Howard, J. A. K. & Puschmann, H. OLEX2: a complete structure solution, refinement and analysis program. *J. Appl. Crystallogr.* **42**, 339–341 (2009).
- Bochevarov, A. D. et al. Jaguar: A high-performance quantum chemistry software program with strengths in life and materials sciences. *Int. J. Quantum Chem.* **113**, 2110–2142 (2013).
- Zhao, Y. & Truhlar, D. G. The M06 suite of density functionals for main group thermochemistry, thermochemical kinetics, noncovalent interactions, excited states, and transition elements: two new functionals and systematic testing of four M06-class functionals and 12 other functionals. *Theor. Chem. Acc.* **120**, 215–241 (2008).
- Grimme, S., Antony, J., Ehrlich, S. & Krieg, H. A consistent and accurate ab initio parametrization of density functional dispersion correction (DFT-D) for the 94 elements H-Pu. *J. Chem. Phys.* **132**, 154104–154119 (2010).
- Goerigk, L. & Grimme, S. A thorough benchmark of density functional methods for general main group thermochemistry, kinetics, and noncovalent interactions. *PCCP* **13**, 6670–6688 (2011).

52. Hay, P. J. & Wadt, W. R. Abinitio effective core potentials for molecular calculations - potentials for K to Au including the outermost core orbitals. *J. Chem. Phys.* **82**, 299–310 (1985).
53. Olsson, M. H. M. & Warshel, A. Solute solvent dynamics and energetics in enzyme catalysis: The S_N2 reaction of dehalogenase as a general benchmark. *J. Am. Chem. Soc.* **126**, 15167–15179 (2004).
54. Berendsen, H. J. C., Vanderspoel, D. & Vandrunen, R. Gromacs - a message-passing parallel molecular-dynamics implementation. *Comput. Phys. Commun.* **91**, 43–56 (1995).
55. King, G. & Warshel, A. A surface constrained all-atom solvent model for effective simulations of polar solutions. *J. Chem. Phys.* **91**, 3647–3661 (1989).
56. Blaha-Nelson, D., Kruger, D. M., Szeler, K., Ben-David, M. & Kamerlin, S. C. L. Active site hydrophobicity and the convergent evolution of paraoxonase activity in structurally divergent enzymes: the case of serum paraoxonase 1. *J. Am. Chem. Soc.* **139**, 1155–1167 (2017).
57. Lemkul, J. A. & Bevan, D. R. Assessing the stability of alzheimer's amyloid protofibrils using molecular dynamics. *J. Phys. Chem. B* **114**, 1652–1660 (2010).
58. Kumar, S., Bouzida, D., Swendsen, R. H., Kollman, P. A. & Rosenberg, J. M. The weighted histogram analysis method for free-energy calculations on biomolecules. I. The method. *J. Comput. Chem.* **13**, 1011–1021 (1992).

Acknowledgements

We would like to thank National Natural Science Foundation of China (21771098 and 21777045), the State Key Laboratory of Fine Chemicals (KF1802), Shenzhen R&D Fund (KQTD20180411143418361), Guangdong Provincial Key Laboratory of Energy Materials for Electric Power (2018B030322001), the Swedish Research Council (2017-00935), the Knut and Alice Wallenberg Foundation (KAW 2016.0072), and the China Scholarship Council (CSC). All calculations were performed on resources provided by the Swedish National Infrastructure for Computing (SNIC) at the National Supercomputing Center in Linköping, Sweden.

Author contributions

J.Y. and L.W. performed experiments. S.Z. and M.S.G.A. performed the computational calculations. H.Z. and H.C. contributed to the discussion of the paper. L.D. and L.S. conceived and directed the project and wrote the paper. All authors discussed the results and commented on the manuscript.

Funding

Open Access funding provided by Kungliga Tekniska Hogskolan.

Competing interests

The authors declare no competing interests.

Additional information

Supplementary information is available for this paper at <https://doi.org/10.1038/s41467-020-20637-8>.

Correspondence and requests for materials should be addressed to L.D. or L.S.

Peer review information *Nature Communications* thanks Javier Concepcion and the other, anonymous, reviewer(s) for their contribution to the peer review of this work.

Reprints and permission information is available at <http://www.nature.com/reprints>

Publisher's note Springer Nature remains neutral with regard to jurisdictional claims in published maps and institutional affiliations.



Open Access This article is licensed under a Creative Commons Attribution 4.0 International License, which permits use, sharing, adaptation, distribution and reproduction in any medium or format, as long as you give appropriate credit to the original author(s) and the source, provide a link to the Creative Commons license, and indicate if changes were made. The images or other third party material in this article are included in the article's Creative Commons license, unless indicated otherwise in a credit line to the material. If material is not included in the article's Creative Commons license and your intended use is not permitted by statutory regulation or exceeds the permitted use, you will need to obtain permission directly from the copyright holder. To view a copy of this license, visit <http://creativecommons.org/licenses/by/4.0/>.

© The Author(s) 2021